

Design Guidelines for Multi-Loop Perturbative Maximum Power Point Tracking Algorithms

J. Kivimäki, *Student Member, IEEE*, S. Kolesnik, *Student Member, IEEE*, M. Sitbon, *Student Member, IEEE*, T. Suntio, *Senior Member, IEEE*, and A. Kuperman, *Senior Member, IEEE*

Abstract—Due to relatively good performance and simple implementation, fixed-step direct maximum power point tracking techniques such as perturb & observe and incremental conductance are the most popular algorithms aimed to maximize the energy yield of photovoltaic energy conversion systems. In order to optimize maximum power point tracking process performance, two design parameters – perturbation frequency and perturbation step size – need to be set a priori, taking into account the properties of both interfacing power converter and photovoltaic generator. While perturbation frequency is limited by the combined energy conversion system settling time, perturbation step size must be high enough to differentiate system response from that caused by irradiation variation. Recent studies have provided explicit design guidelines for single-loop maximum power point tracking structures only, where the algorithm directly sets the interfacing converter duty cycle. It was shown that dynamic resistance of the photovoltaic generator, which is both operation point and environmental conditions dependent, significantly affects the combined energy conversion system settling time. On the other hand, no design guidelines were explicitly given for multi-loop maximum power point tracking structures, where the algorithm sets the reference signal for photovoltaic generator voltage and inner voltage controller performs the regulation task. This paper introduces perturbation frequency and perturbation step size design guidelines for such systems. It is shown that while perturbation step size design is similar to that of single-loop structures, perturbation frequency design is quite different. It is revealed that once the inner voltage loop is properly closed, the influence of photovoltaic generator dynamic resistance on settling time (and thus on perturbation frequency design) is negligible. Experimental results are provided to verify the proposed guidelines validity.

Index Terms—Maximum power point tracking, perturbative algorithms, multi-loop control structure.

I. INTRODUCTION

SOLAR energy conversion systems are usually operated either at maximum power point (MPP) [1-3] in order to harvest as much energy as possible or at limited power point (LPP) to match the photovoltaic generator (PVG) with load capable of utilizing only partial amount of harvested energy [4-7]. Fixed step perturb and observe (P&O) and incremental conductance (IC) are probably the most frequently used MPP tracking (MPPT) methods, both related to the class of perturbative (or direct) algorithms. There, a perturbation Δx is injected into the system by the MPPT algorithm every ΔT seconds. Following a transient lasting T_Δ seconds (cf. Fig. 1), the polarity (and sometimes size) of corresponding optimization function (i.e. PVG power in P&O method and sum of static and dynamic conductances in IC method) change $\Delta y[k] = y[k] - y[k-1]$ is detected. The information is then used to determine the polarity (and sometimes size) of the next

perturbation in order to drive the operation point towards MPP [1]. The two design parameters to be decided on are then perturbation period ΔT and step size Δx . In case of fixed-step MPPT algorithms, the two are determined once a priori and remain unchanged during the operation.

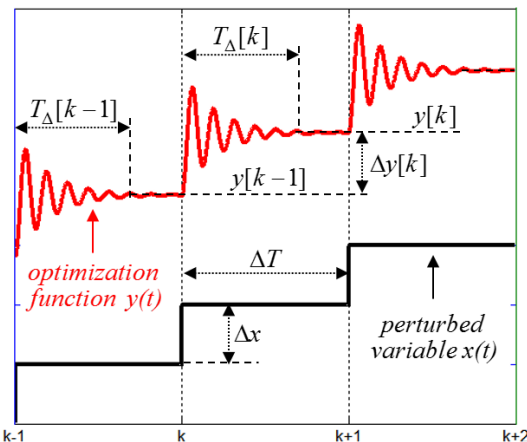


Fig. 1. Short-time dynamics of perturbative MPPT methods.

Following [3] and [8], design guidelines may be summarized as follows. Perturbation period should be higher than the longest settling time of the PVG output power transient induced by injected perturbation (i.e. $\Delta T > T_\Delta$ must hold throughout the whole operation range), otherwise the algorithm may be deceived and the operating point can enter a chaotic behavior. Perturbation step size influences the MPPT algorithm performance in both stationary and time-varying atmospheric conditions [9]. In general, perturbation step size should be reduced to increase the efficiency under stationary environmental conditions. However, it must remain high enough so that corresponding optimization function change would be higher than that caused by the maximum possible irradiation variation to prevent convergence failure.

Due to the highly nonlinear PVG characteristics and varying environmental conditions in terms of irradiance and ambient temperature, dynamics of solar energy conversion system must be properly identified for each possible operation point. The I-V curve of a PVG (cf. Fig. 2) for given environmental conditions is typically divided into two sections, separated by the MPP: constant current (CCR) region, corresponding to voltages below the MPP voltage, and constant voltage (CVR) region, belonging to voltages above the MPP voltage. Each region is named according to the variable, remaining practically constant within the relevant section [10]-[12]. However, due to finite resolution of digitally controlled measurement systems, MPP is a region rather than a single point. Therefore, I-V curve section at the vicinity of

MPP may be entitled as constant-power region (CPR), as shown in Fig. 2 (CPR existence was utilized in ripple correlation control MPPT algorithm [13]). Moreover, low-frequency PVG dynamic resistance (r_{pv}) correlates well with corresponding practical electrical source of each region (high in CCR, low in CVR) [14]. At MPP, static (R_{pv}) and dynamic resistances are equal [15].

Two main MPPT control structures are typically adopted [8],[9]. The first one (related to as single-loop) involves direct perturbation of the interfacing power converter (IPC) duty cycle, as shown in Fig. 3a. After duty cycle perturbation, the system operates in open loop. In the second, one (further related to as multi-loop), the MPPT algorithm perturbs the PVG reference voltage while input voltage controller (IVC) ensures correct tracking by appropriately varying the IPC duty cycle (see Fig. 3b). While the former is simpler and usually faster (for the same control bandwidth), the latter is often preferred due to improved robustness to irradiation changes [16], [17].

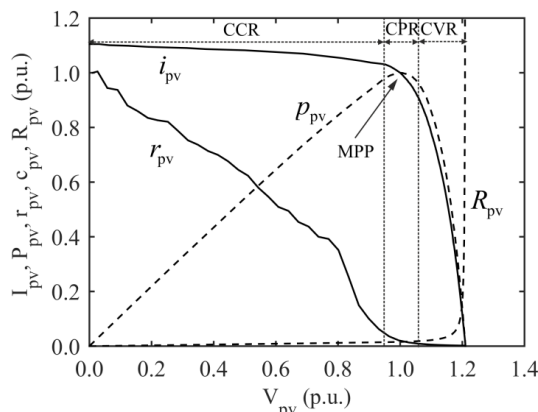


Fig. 2. Normalized static behavior of PVG current i_{pv} , power p_{pv} , dynamic resistance r_{pv} , and static resistance R_{pv} as function of PVG voltage v_{pv} . Currents and voltages are normalized according to respective PVG MPP values while resistances are normalized according to their peak values.

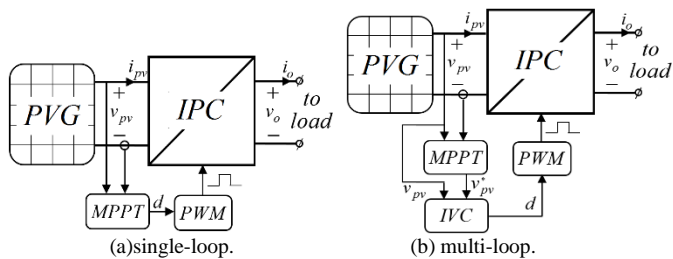


Fig. 3. MPPT control structures.

Most of case studies in the literature follow the generalized guidelines given in [3] and [8], where perturbation period and step size of direct MPPT algorithms are recommended to be selected at MPP, corresponding to standard test conditions (1000W/m² irradiation and 25°C temperature). However, it is well known that PVG dynamic resistance significantly affects the dynamic behavior of combined solar energy conversion system by modifying the open-loop damping factor [11,14,18,19]. The latter is inversely proportional to PVG dynamic resistance; hence damping is lessened when operating point moves to CCR (cf. Fig. 2) due to high value of dynamic resistance and minimized at short-circuit condition.

In case of single-loop MPPT control structure, this implies longest PVG-power-transient-settling time in CCR. Thus, as recently revealed in [20], perturbation period must be determined in CCR rather than at MPP (or CPR). On the other hand, selecting proper perturbation step magnitude should still be carried out at MPP (or CPR) as shown in [3]. Experimental normalized transient waveforms of Raloss SR30-36 PVG [14], interfaced by single-loop MPPT operated boost-type IPC, are shown in Fig. 4 [20], confirming the validity of the above findings. Apparently, PVG power settling time is longest in CCR.

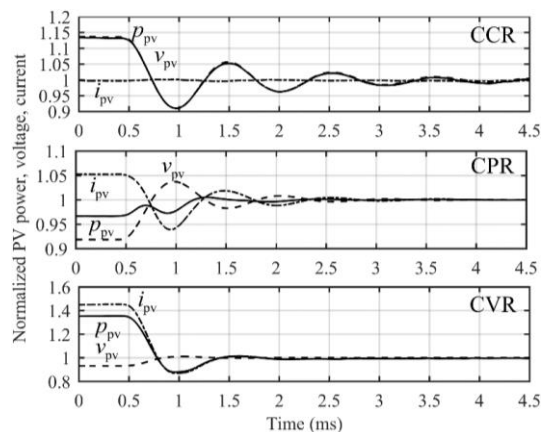


Fig. 4. Behavior of PVG voltage, current, and power upon duty ratio step change applied to a single-loop MPPT operated boost-type IPC. All the original waveforms were normalized to their final values to maximize the information of the settling behavior.

It must be emphasized that design guidelines given in [3] and [8] seem to be generalized and intended for both MPPT structures of Fig. 3. Nevertheless, there is no evidence in the literature (including [3] and [8]) of applying these to systems employing multi-loop MPPT structures. For example, the authors of [21] recommend determining minimum allowed perturbation period by means of simulations rather than analytically. In [22], perturbation frequency was set to less than one-tenth of the input-voltage-feedback-loop crossover frequency without justification. Consequently, this paper aims to fulfil the gap by demonstrating that in case the input-voltage feedback loop is properly closed, PVG-power-settling time would be independent of PVG dynamic resistance, thus being longest in CPR. Revealed analytical findings are experimentally validated utilizing boost IPC-based solar energy conversion system [18].

It should be highlighted that the paper only treats the case where input voltage controller (IVC, cf. Fig. 3b) directly sets the converter duty cycle. In case of cascaded input-voltage-feedback implementation (i.e. including current-mode control as in [23],[24]), dependence on the PVG properties may still exist and the outcomes presented in this paper may not be valid (future work would reveal the details).

The rest of the paper is organized as follows. Small-signal dynamics of the solar energy conversion system is developed in Section II. Section III reveals the rules for perturbation frequency and step size design. Design example utilizing the proposed technique is discussed in Section IV and experimentally validated in Section V. The conclusions are drawn in Section VI.

II. GENERAL DYNAMICS OF PVG POWER

General representation of a solar energy conversion system is presented in Fig. 5(a), where the IPC (either of DC-DC or DC-AC type) is represented by a two-terminal (IN/OUT) subsystem, terminated by a downstream system. Power grid, grid-connected inverter or storage battery may usually realize the latter. Corresponding small-signal representation of the combined system is shown Fig. 5(b), where \hat{i}_{ph} and $Y_{pv} = 1/r_{pv}$ are the small-signal PVG Norton equivalents [11], [25]. PVG dynamic conductance Y_{pv} is obtained from a corresponding I-V curve by

$$Y_{pv} = 1/r_{pv} = -\frac{\partial i_{pv}}{\partial v_{pv}}. \quad (1)$$

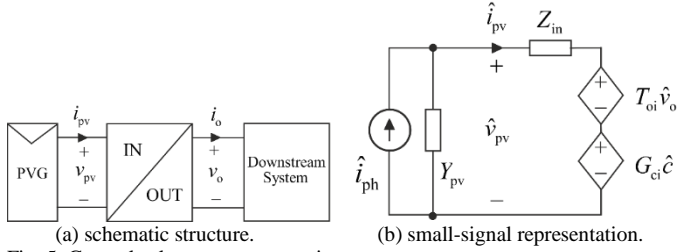


Fig. 5. General solar energy conversion system.

Moreover, \hat{c} denotes the general control variable (i.e., PVG voltage reference in case of multi-loop MPPT structure); $G_{ci}(s)$, $T_{oi}(s)$ and $Z_{in}(s)$ represent closed-loop IPC control-to-input voltage transfer function, closed-loop output-to-input voltage transfer function, and closed-loop IPC input impedance, respectively. According to Fig. 5(b), combined PVG-IPC dynamics satisfies

$$\begin{aligned} \hat{v}_{pv} &= \frac{Z_{in}}{1 + Z_{in}Y_{pv}} \hat{i}_{ph} + \frac{T_{oi}}{1 + Z_{in}Y_{pv}} \hat{v}_o + \frac{G_{ci}}{1 + Z_{in}Y_{pv}} \hat{c} \\ \hat{i}_{pv} &= \frac{1}{1 + Z_{in}Y_{pv}} \hat{i}_{ph} - \frac{Y_{pv}T_{oi}}{1 + Z_{in}Y_{pv}} \hat{v}_o - \frac{Y_{pv}G_{ci}}{1 + Z_{in}Y_{pv}} \hat{c}. \end{aligned} \quad (2)$$

Note that once $Z_{in}Y_{pv} \ll 1$ within the control bandwidth, PVG dynamic resistance influence on the system dynamics is minimized. This is achieved by properly closing the input voltage loop, as shown later on.

It is well known that PVG temperature significantly affects the output power yet its dynamics is quite slow due to the large thermal capacity of solar panels. Therefore, temperature effect is not considered in (2), similarly to [3]. For perturbation period design, the control-to-PVG voltage dynamics

$$T(s) = \frac{G_{ci}(s)}{1 + Z_{in}(s)Y_{pv}} = \frac{\hat{v}_{pv}}{\hat{c}}(s) \Bigg|_{\hat{c}=\hat{v}_{pv}^*} = \frac{C(s)P(s)}{1 + C(s)P(s)} \quad (3)$$

with $P(s) = \frac{\hat{v}_{pv}}{\hat{a}}(s)$ and $C(s)$ denoting open-loop PVG voltage loop plant and controller, respectively, is of interest in (2).

Perturbing PVG power, voltage and current as $p_{pv} = P_{pv} + \hat{p}_{pv} = (V_{pv} + \hat{v}_{pv})(I_{pv} + \hat{i}_{pv})$, small-signal dynamics of the former is derived as [3]

$$\hat{p}_{pv} = I_{pv}\hat{v}_{pv} + V_{pv}\hat{i}_{pv} + \hat{i}_{pv}\hat{v}_{pv}. \quad (4)$$

Considering that dynamics of PVG power is caused by a step change in PVG voltage, (4) may be rewritten as [11]

$$\hat{p}_{pv} \approx V_{pv} \left(\frac{1}{R_{pv}} - \frac{1}{r_{pv}} \right) \hat{v}_{pv} - \frac{1}{r_{pv}} \hat{v}_{pv}^2 \quad (5)$$

since (cf. (1))

$$\hat{i}_{pv} \approx -\frac{1}{r_{pv}} \hat{v}_{pv}, \quad R_{pv} = \frac{V_{pv}}{I_{pv}}. \quad (6)$$

According to (2), (5) and the discussion in Introduction section, PVG power ripple may hence be approximated by

$$\hat{p}_{pv}(t) \approx I_{pv}\hat{v}_{pv}(t) = I_{pv}L^{-1}\{\hat{v}_{pv}^*(s)T(s)\} \quad (7a)$$

in CCR ($L^{-1}\{\}$ denotes inverse Laplace transform operator), since $r_{pv} \gg R_{pv}$ holds there;

$$\hat{p}_{pv}(t) \approx V_{pv}\hat{i}_{pv}(t) = -\frac{V_{pv}}{r_{pv}}\hat{v}_{pv}(t) = -\frac{V_{pv}}{r_{pv}}L^{-1}\{\hat{v}_{pv}^*(s)T(s)\} \quad (7b)$$

in CVR, since $r_{pv} \ll R_{pv}$ in this region; and

$$\hat{p}_{pv}(t) \approx -\frac{1}{R_{pv}}\hat{v}_{pv}^2(t) = -\frac{1}{R_{pv}}\left(L^{-1}\{\hat{v}_{pv}^*(s)T(s)\}\right)^2 \quad (7c)$$

in CPR, where R_{pv} and r_{pv} are close. Fig. 6 demonstrates the effect of sinusoidal PVG voltage perturbation on PVG power for Raloss SR30-36 PVG. Power ripple behavior clearly follows the formulations given above (i.e., the ripple is nearly-constant and in phase with the PVG voltage ripple in CCR; the ripple increases with the increase in PVG voltage and is in opposite phase with the PVG voltage ripple in CVR; the ripple is close to zero in CPR). Fig. 6 also validates CPR existence, discussed in the Introduction section.

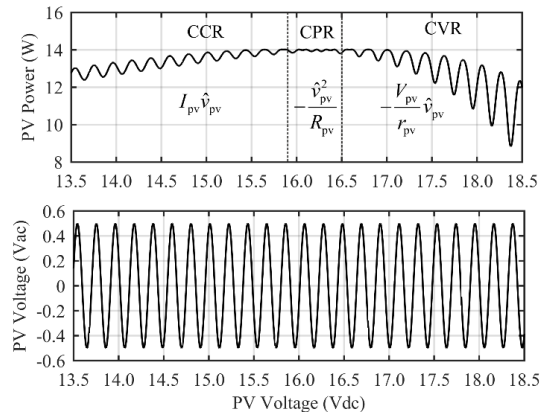


Fig. 6. Extended view of PVG voltage induced PVG power ripple at the vicinity of CPR.

III. MPPT PERTURBATION PARAMETERS DESIGN

A. Perturbation frequency design

Generalized open-loop PVG voltage loop plant (cf. (3)) of a combined PVG-IPC system may be expressed as an underdamped second-order transfer function of the following form [3],[8]

$$P(s) = G \frac{\omega_n^2 (1 + \omega_z^{-1}s)}{s^2 + 2\zeta_n \omega_n s + \omega_n^2} \quad (8)$$

with G , ω_n , ζ_n and ω_z denoting DC gain, undamped natural frequency, damping factor and capacitor ESR induced zero, respectively. As shown in [11],[18],[19], while PVG dynamic resistance greatly affects the damping factor, its influence on the DC gain and natural frequency is insignificant. The crossover frequency of $P(s)$ is given by

$$\omega_p = \omega_n \sqrt{(1-4\zeta_n^2) \left(1 + \sqrt{1 + \left(\frac{G}{1-4\zeta_n^2} \right)^2} \right)} \quad (9)$$

$$\approx \omega_n \sqrt{G} \Big|_{\zeta_n \ll 1, G \gg 1},$$

while resonant frequency and corresponding gain are obtained as

$$\omega_0 \approx \omega_n \sqrt{1-2\zeta_n^2}, \quad |P(j\omega_0)| \approx \frac{G}{2\zeta_n \sqrt{1-\zeta_n^2}}. \quad (10)$$

Two classical ways exist to compensate (8). In case the desired loop gain crossover frequency ω_c is much lower than ω_p , integral (I) controller of the form

$$C_i(s) = \frac{\omega_c}{\bar{G}s(1+\omega_z^{-1}s)} \quad (11)$$

is typically used with \bar{G} denoting the nominal value of G . In case $\omega_c \ll \omega_z$, there is no need to cancel the capacitor ESR induced zero and pure integrator may be utilized. The loop gain is then given by

$$LG_i(s) = C_i(s)P(s) = \frac{G\bar{G}^{-1}\omega_c}{s} \frac{\omega_n^2}{s^2 + 2\zeta_n\omega_n s + \omega_n^2} \quad (12a)$$

and may be approximated as

$$LG_i(s) \approx \frac{G\bar{G}^{-1}\omega_c}{s}, \quad 0 < \omega < \omega_c \quad (12b)$$

within the control bandwidth. Since the plant is underdamped, loop gain resonance peak must reside GM [dB] (gain margin) below zero to assure stability. Hence, loop gain crossover frequency must satisfy

$$G\bar{G}^{-1}\omega_c < 10^{\frac{GM}{20}} \omega_n \zeta_n (1-2\zeta_n^2). \quad (13)$$

PVG voltage loop complementary sensitivity function (cf. (3)) may then be approximated within the control bandwidth as

$$T_i(s) = \frac{LG_i(s)}{1+LG_i(s)} \approx \frac{G\bar{G}^{-1}\omega_c}{s+G\bar{G}^{-1}\omega_c} = T_i^a(s), \quad 0 < \omega < \omega_c. \quad (14)$$

Hence, following (7) and assuming

$$\hat{v}_{pv}^*(s) = \frac{\Delta V_{pv}^*}{s}, \quad (15)$$

PVG power ripple is obtained as

$$\hat{p}_{pv,i}(t) \approx I_{pv} L^{-1} \left\{ \hat{v}_{pv}^*(s) T_i^a(s) \right\} \\ = I_{pv} \Delta V_{pv}^* \left(1 - \exp(-G\bar{G}^{-1}\omega_c t) \right) \quad (16a)$$

in CCR,

$$\hat{p}_{pv,i}(t) \approx -\frac{V_{pv}}{r_{pv}} L^{-1} \left\{ \hat{v}_{pv}^*(s) T_i^a(s) \right\} \\ = -\frac{V_{pv}}{r_{pv}} \Delta V_{pv}^* \left(1 - \exp(-G\bar{G}^{-1}\omega_c t) \right) \quad (16b)$$

in CVR and

$$\hat{p}_{pv,i}(t) \approx -\frac{1}{R_{pv}} \left(L^{-1} \left\{ \hat{v}_{pv}^*(s) T_i^a(s) \right\} \right)^2 \\ \approx -\frac{\Delta V_{pv}^*}{R_{pv}} \left(1 - 2\exp(-G\bar{G}^{-1}\omega_c t) \right) \quad (16c)$$

in CPR (the higher order term was neglected in (16c) similarly to [8]). Settling times within $\pm\Delta$ band around corresponding steady-state value are then given by

$$T_\Delta = \frac{1}{G\bar{G}^{-1}\omega_c} \ln \left(\frac{1}{\Delta} \right) \quad (17a)$$

in CCR and CVR, and by

$$T_\Delta = \frac{1}{G\bar{G}^{-1}\omega_c} \ln \left(\frac{2}{\Delta} \right) \quad (17b)$$

in CPR. Consequently, once $G\bar{G}^{-1}$ is close to unity, settling time in CPR is expected to be slightly longer than in CCR and CVR.

In case the desired loop gain crossover frequency ω_c is close to or higher than ω_p , proportional-derivative-integral (PID) controller of the form

$$C_{pid}(s) = \frac{\omega_c}{\bar{G}\bar{\omega}_n^2 s} \frac{s^2 + 2\bar{\omega}_n s + \bar{\omega}_n^2}{(1+\omega_z^{-1}s)(1+\omega_f^{-1}s)} \quad (18)$$

is typically used with $\bar{\omega}_n$ denoting the nominal value of ω_n . Additional pole ω_f is usually placed between one-tenth to half the switching frequency to suppress high-frequency noise. The loop gain is then given by

$$LG_{pid}(s) = C_{pid}(s)P(s) \\ = \frac{G\bar{G}^{-1}\omega_n^2 \bar{\omega}_n^{-2} \omega_c}{s(1+\omega_f^{-1}s)} \frac{s^2 + 2\bar{\omega}_n s + \bar{\omega}_n^2}{s^2 + 2\zeta_n \omega_n s + \omega_n^2} \exp(-T_d s), \quad (19)$$

taking into account delay T_d caused by sampling and PWM modulator. PVG voltage loop complementary sensitivity function is then obtained as a fourth-order unity-DC-gain system with relative degree of two and may hence be approximated within the control bandwidth by a dominant pole pair as

$$T_{pid}(s) = \frac{LG_{pid}(s)}{1+LG_{pid}(s)} \approx \frac{\omega_a^2}{s^2 + 2\zeta_a \omega_a s + \omega_a^2} = T_{pid}^a(s), \quad 0 < \omega < \omega_c. \quad (20)$$

Several methods exist for such a model reduction. Here, classical control engineering related approach is used as follows. Once $T_{pid}(s)$ is well-approximated by $T_{pid}^a(s)$, the loop gain may be expressed by

$$LG_{pid}(s) \approx \frac{T_{pid}^a(s)}{1-T_{pid}^a(s)} = \frac{\omega_a^2}{s(s+2\zeta_a \omega_a)}, \quad 0 < \omega < \omega_c. \quad (21)$$

For such a system, crossover frequency ω_c and phase margin PM are given by [26]

$$\omega_c = \omega_a \sqrt{\sqrt{1+4\zeta_a^4} - 2\zeta_a^2}, \quad \text{PM} = \tan^{-1} \left(\frac{2\zeta_a}{\sqrt{\sqrt{1+4\zeta_a^4} - 2\zeta_a^4}} \right) \quad (22)$$

(16b) Consequently, reduced model parameters may be obtained as

$$\omega_a = \frac{\omega_c}{\sqrt{\sqrt{1+4\zeta_a^4} - 2\zeta_a^2}}, \quad \zeta_a = \frac{\tan(\text{PM})}{2(1+\tan^2(\text{PM}))^{\frac{1}{4}}}. \quad (23)$$

Taking into account (7) and (15), PVG power ripple is obtained as

IEEE TRANSACTIONS ON POWER ELECTRONICS

$$\begin{aligned} \hat{p}_{pv,pid}(t) &\approx I_{pv} L^{-1} \left\{ \hat{v}_{pv}^* T_{pid}^a(s) \right\} \\ &= I_{pv} \Delta V_{pv}^* \left(1 \pm \frac{1}{\sqrt{1-\zeta_a^2}} \exp(-\zeta_a \omega_a t) \cdot \sin \theta(t) \right) \end{aligned} \quad (24a)$$

in CCR,

$$\begin{aligned} \hat{p}_{pv,pid}(t) &\approx -\frac{V_{pv}}{r_{pv}} L^{-1} \left\{ \hat{v}_{pv}^*(s) T_{pid}^a(s) \right\} \\ &= -\frac{V_{pv}}{r_{pv}} \Delta V_{pv}^* \left(1 \pm \frac{1}{\sqrt{1-\zeta_{pv}^2}} \exp(-\zeta_{pv} \omega_n t) \cdot \sin \theta(t) \right) \end{aligned} \quad (24b)$$

in CVR and

$$\begin{aligned} \hat{p}_{pv,pid}(t) &\approx -\frac{1}{R_{pv}} \left(L^{-1} \left\{ \hat{v}_{pv}^*(s) T_i^a(s) \right\} \right)^2 \\ &\approx -\frac{\Delta V_{pv}^*}{R_{pv}} \left(1 - 2 \frac{1}{\sqrt{1-\zeta_{pv}^2}} \exp(-\zeta_{pv} \omega_n t) \cdot \sin \theta(t) \right) \end{aligned} \quad (24c)$$

in CPR with $\theta(t) = \omega_a \sqrt{1-\zeta_a^2} t + \tan^{-1} \left\{ \frac{\sqrt{1-\zeta_a^2}}{\zeta_a} \right\}$ (again, the

higher order term was neglected in (24c) as in [8]). Consequently, settling times are determined from the corresponding power ripple envelopes, given by

$$env(\hat{p}_{pv,pid}) = -I_{pv} \Delta V_{pv}^* \left(1 \pm \frac{1}{\sqrt{1-\zeta_a^2}} \exp(-\zeta_a \omega_a t) \right) \quad (25a)$$

in CCR,

$$env(\hat{p}_{pv,pid}) = -\frac{V_{pv}}{r_{pv}} \Delta V_{pv}^* \left(1 \pm \frac{1}{\sqrt{1-\zeta_a^2}} \exp(-\zeta_a \omega_a t) \right) \quad (25b)$$

in CVR, and

$$env(\hat{p}_{pv,pid}) \approx -\frac{\Delta V_{pv}^*}{R_{pv}} \left(1 \pm 2 \frac{1}{\sqrt{1-\zeta_a^2}} \exp(-\zeta_a \omega_a t) \right) \quad (25c)$$

in CPR. Settling times within $\pm\Delta$ band around corresponding steady-state value are then given by

$$T_{\Delta} = \frac{1}{\zeta_a \omega_a} \ln \left(\frac{1}{\Delta \sqrt{1-\zeta_a^2}} \right) \quad (26a)$$

in CCR and CVR, and by

$$T_{\Delta} \approx \frac{1}{\zeta_a \omega_a} \ln \left(\frac{2}{\Delta \sqrt{1-\zeta_a^2}} \right) \quad (26b)$$

in CPR. According to the factor of 2 in (26b), the settling time in CPR is expected to be the longest.

B. Perturbation step size design

As discussed in [3,8,27], perturbation step size should be to be reduced as long as the change in the PVG power induced by the perturbation step is higher than that induced by irradiation change. The design process was carried out in [3,8] for single-loop MPPT structures. It was shown that duty cycle (which is the control input in case of a system with single-loop MPPT structure) perturbation must satisfy the following relation,

$$\Delta d > \frac{1}{G_0} \sqrt{\frac{V_{pv,MPP} \cdot K_{ph} \cdot |\dot{G}_s| \cdot \Delta T}{H \cdot V_{pv,MPP} + r_{pv,MPP}^{-1}}}, \quad (27)$$

where subscript "MPP" symbolizes Standard Test Conditions corresponding MPP, $K_{ph} = \frac{\partial i_{pv}}{\partial G_s}$ denotes PVG material constant, G_0 is DC gain of duty cycle – to – PVG voltage transfer function $\frac{v_{pv}}{d}(s)$, G_s represents solar irradiation and $H = -\frac{1}{2} \frac{\partial^2 i_{pv}}{\partial^2 v_{pv}} \Big|_{MPP}$. It is important to emphasize that since H , $V_{pv,MPP}$ and $r_{pv,MPP}$ depend on environmental conditions, the combination of parameters leading to the highest value of Δd must be utilized while the worst case of irradiation change rate is usually assumed to be 100 [W·m⁻²·s⁻¹]. In addition to irradiation variations, finite resolution of utilized analog-digital converter (ADC) should also be taken into account [8], [20].

In case of multi-loop MPPT structure, PVG voltage reference (cf. Fig. 3b) is the control input. Therefore, multiplying both sides of (27) by G_0 yields

$$\Delta v_{pv}^* > \sqrt{\frac{V_{pv,MPP} \cdot K_{ph} \cdot |\dot{G}_s| \cdot \Delta T}{H \cdot V_{pv,MPP} + r_{pv,MPP}^{-1}}} \quad (28)$$

since DC gain of closed voltage loop $\frac{v_{pv}}{v_{pv}^*}(s)$ is unity. Issues related to environmental dependence of (28) as well to finite resolution effects apply to (28) as well.

IV. DESIGN EXAMPLE

Consider a solar energy conversion system, consisting of a diode rectification boost type IPC, fed by Raloss SR30-36 PVG and terminated by a 24V, 7.2Ah lead-acid battery, held at 26V to realize a near-ideal voltage source, as shown in Fig. 7, also demonstrating simplified control system and measurement interface. It should be noted that the obtained results are also valid for synchronous rectification boost type IPC, possessing higher efficiency and enhanced thermal performance [28].

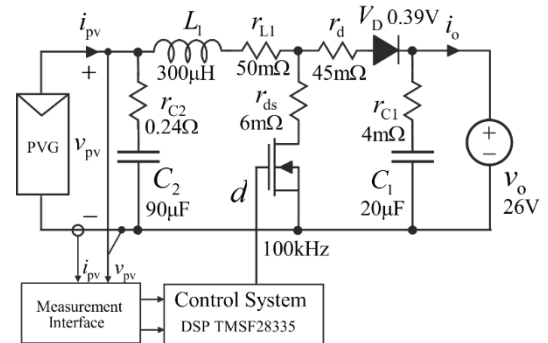


Fig. 7. Solar energy conversion system under study.

Raloss SR30-36 module consists of 36 series-connected mono-crystalline silicon cells. The PVG was illuminated by fluorescent lamps, capable of producing 500 W/m² irradiance, yielding PVG short-circuit current and open-circuit voltage of 1 A and 19.2 V, respectively, at panel temperature of 45 °C. Detailed characterization of the PV panel and modeling of boost-type IPC can be found in [14] and [18], respectively.

IEEE TRANSACTIONS ON POWER ELECTRONICS

Three operating points, in which transient behavior of PVG power is analyzed, are 1.0 A & 12 V in CCR, 0.91 A & 16 V in CPR, and 0.61 A & 18 V in CVR. The values of PVG dynamic resistance r_{pv} are estimated as 1000 Ω in CCR, 17.6 Ω in CPR and 3.5 Ω in CVR. The IPC/control system was operated with switching/sampling frequency of $f_s = 100$ kHz.

Following [18], the open-loop PVG voltage loop plant of the combined PVG-IPC system is given by (8), where

$$G = -\frac{V_e r_{pv}}{r_{pv} + R_e - r_{C2}}, \omega_n^2 = \frac{r_{pv} + R_e - r_{C2}}{L_1 C_2 (r_{pv} + r_{C2})}, \omega_z = \frac{1}{r_{C2} C_2} \quad (29a)$$

$$\zeta_n = \frac{L_1 + C_2 (R_e r_{pv} + r_{C2} (R_e - r_{C2}))}{2\sqrt{(L_1 C_2 (r_{pv} + r_{C2})) (r_{pv} + R_e - r_{C2})}}$$

with

$$V_e = V_o + V_D + (r_d - r_{ds}) I_{pv}, \quad (29b)$$

$$R_e = r_{L1} + r_{C2} + D r_{ds} + (1 - D) r_d.$$

and D , I_{pv} symbolizing steady-state values of converter duty cycle and PVG current, respectively. Calculated numerical values of the combined PVG-IPC system in each region are summarized in Table I. Apparently, PVG influence is mainly reflected by the damping factor.

TABLE I
CALCULATED NUMERICAL VALUES OF THE COMBINED PVG-IPC SYSTEM IN EACH REGION

	ω_n , rad/s	ζ_n	$-G$, V	ω_p , rad/s	ω_0 , rad/s	$ P(j\omega_0) _s$, dB	ω_z , rad/s
CCR	6085	0.096	26.43	31283	6029	42.8	46296
CPR	6057	0.136	26.32	31073	5944	39.8	46296
CVR	5957	0.301	26.01	30397	5391	33.1	46296

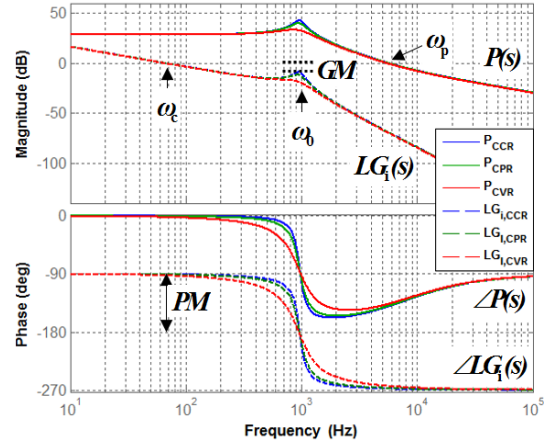
Nominal values of G and ω_n are then selected as

$$\bar{G} = \frac{G_{CCR} + G_{CPR} + G_{CVR}}{3}, \quad \bar{\omega}_n = \frac{\omega_{n,CCR} + \omega_{n,CPR} + \omega_{n,CVR}}{3}. \quad (30)$$

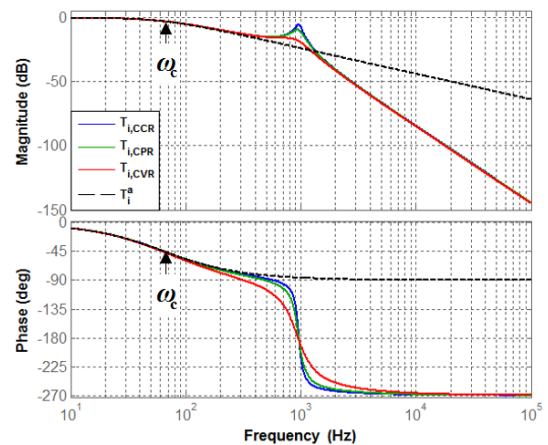
A. $\omega_c \ll \omega_p$

For the case of desired loop gain crossover frequency ω_c is much lower than ω_p , integral (I) controller (11) was used. Since the plant is underdamped, the worst case resonance peak of the loop gain must reside GM [dB] below zero to assure stability (cf. (13)). Hence, CCR operation dictates the loop gain crossover frequency. Selecting gain margin of 6 dB, loop gain crossover frequency is obtained as $\omega_c = 2\pi 50$ rad/s. Moreover, since $\omega_c \ll \omega_z$, there is no need to cancel the capacitor ESR induced zero. Thus, pure integrator was utilized as loop compensator. Bode diagram of the plants $P(s)$ and resulting loop gains $LG_i(s)$ are shown in Fig. 8a for all the three regions. Apparently, the loop gain is well approximated by (12b) within the control bandwidth and the phase margin is $PM \approx 90^\circ$. Bode diagram of the complementary sensitivity functions $T_i(s)$ is shown in Fig. 8b and is well predicted by (14) within the control bandwidth, as expected. Fig. 8c presents step responses of $T_i(s)$ and approximating function $T_i^a(s)$ with $\Delta = 0.05$ (5%) settling times indicated. It may be concluded that the differences are very small, indicating that PVG dynamic resistance has negligible influence on dynamic performance. Hence, following (17), PVG power settling times within 5% band are then expected as

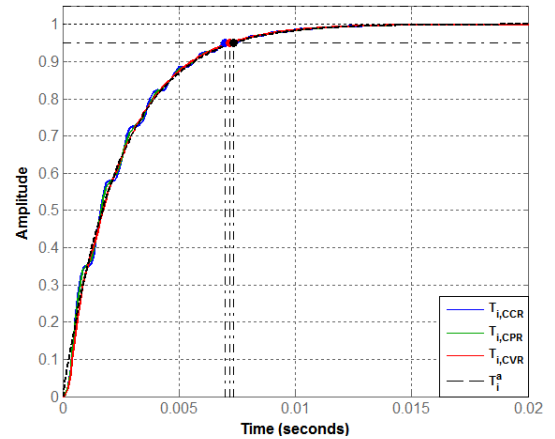
$$T_{\Delta CCR} = T_{\Delta CVR} \approx 9ms, \quad T_{\Delta CPR} \approx 12ms. \quad (31)$$



(a) plant and loop gain Bode diagrams



(b) complementary sensitivity functions Bode diagram



(c) step responses of complementary sensitivity functions

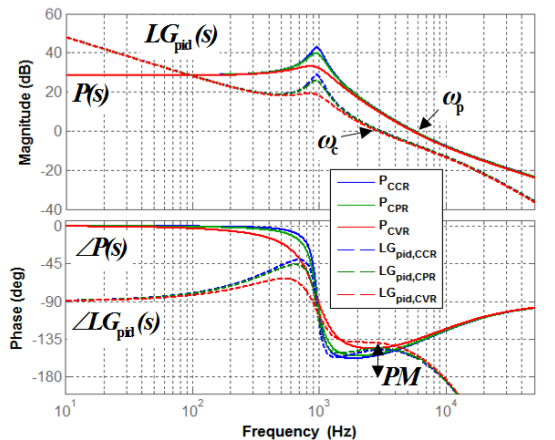
Fig. 8. System analysis under I-control.

B. $\omega_c \approx \omega_p$

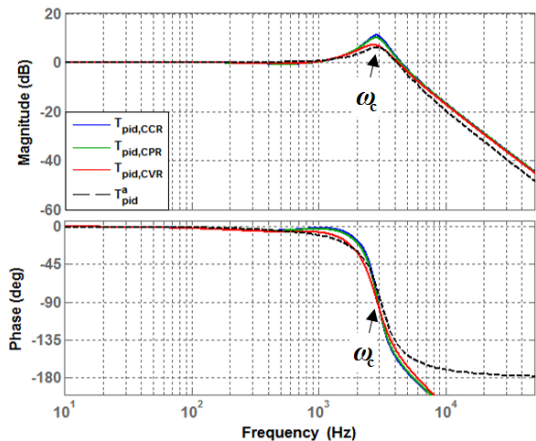
For the case of desired loop gain crossover frequency ω_c close to ω_p , proportional-derivative-integral (PID) controller (18) was used. The additional pole ω_f was placed at one-sixth the switching frequency to suppress high-frequency noise. The loop gain crossover frequency was selected as $2\pi 3000$ rad/s. Bode diagram of the plants $P(s)$ and resulting loop gains $LG_{pid}(s)$ are shown in Fig. 9a for all the three regions. Note that the diagrams account for $T_d = 1.5/f_s$ total switching and

sampling delay. From Fig. 9a, average crossover frequency and phase margin are $2\pi 2950$ rad/s and 35° , respectively. Bode diagram of the complementary sensitivity functions $T_{pid}(s)$ is shown in Fig. 9b and is well predicted within the control bandwidth by (20) with $\omega_a = 20500$ rad/s, $\zeta_a = 0.32$, obtained using (23). Fig. 9c presents step responses of $T_{pid}(s)$ and approximating function $T_{pid}^a(s)$ with $\Delta = 0.05$ (5%) settling times indicated. It may be concluded that the differences are insignificant, indicating that PVG dynamic resistance has minor influence on settling time. Hence, following (17), PVG power settling times within 5% band are then expected as

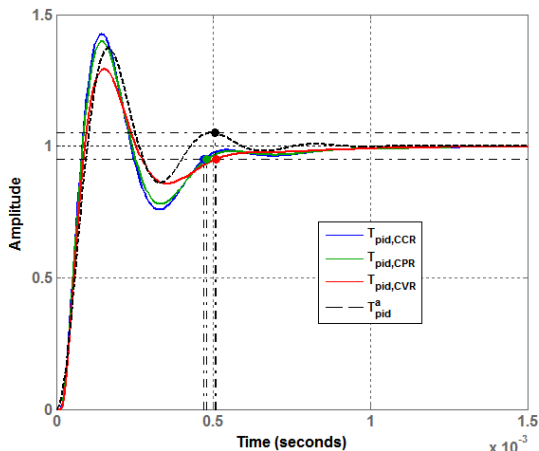
$$T_{\Delta,CCR} = T_{\Delta,CVR} \approx 0.47ms, \quad T_{\Delta,CPR} \approx 0.57ms. \quad (32)$$



(a) plant and loop gain Bode diagrams



(b) complementary sensitivity functions Bode diagram

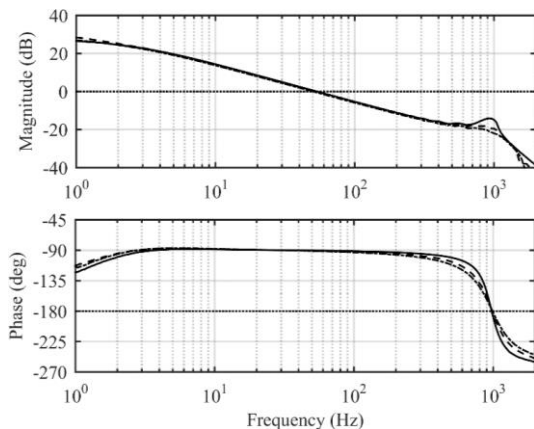


(c) step responses of complementary sensitivity functions

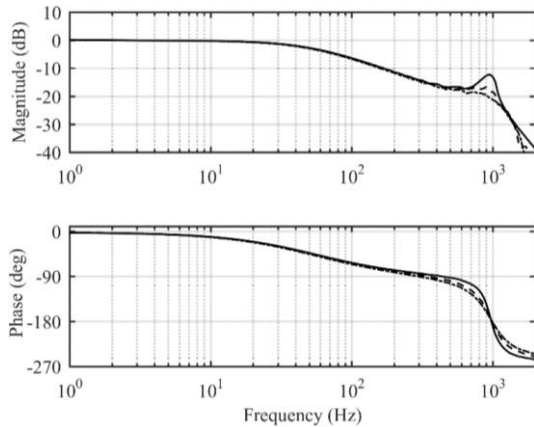
Fig. 9. System analysis under PID-control.

V. EXPERIMENTAL VALIDATION

In order to validate the analytical findings of the previous Section, experimental setup shown in Fig. 6 was built and utilized during the experiments. Frequency responses were obtained by Venable Model 3120 frequency response analyzer; no post-processing was applied. Time domain responses were post-processed by normalization only (original results were divided by corresponding final values for improving the visibility). Measured open and closed loop Bode plots, corresponding to case A of the preceding Section (I-controller, $\omega_c \ll \omega_p$) are presented in Fig. 10 for the three operating regions.



(a) loop gain Bode diagrams



(b) complementary sensitivity functions Bode diagram

Fig. 10. Measured system responses under I-control (CCR: solid line, CPR: dashed line, and CVR: dash-dotted line).

Apparently, measured frequency responses match well the predicted ones (cf. Figs. 8a and 8b) and the fact that PVG resistance has negligible influence on dynamic performance is supported. Fig. 11 presents measured PVG voltage, current, and power responses to a reference PVG voltage step change in the three operating regions under I-control. The results validate the first order transient behavior. Moreover, power behavior satisfies (7) precisely: in CCR, it follows the settling behavior of PVG voltage; in CVR, it correlates with the settling behavior of the PVG current; in CPR, the PVG power transient is very small, since PVG voltage and current transients tend to cancel each other.

Measured open and closed loop Bode plots, corresponding to case B of the preceding Section (PID-controller, $\omega_c \approx \omega_p$)

IEEE TRANSACTIONS ON POWER ELECTRONICS

are presented in Fig. 12 for the three operating regions. Again, measured frequency responses correspond well with the analytically obtained ones (cf. Figs. 9a and 9b). Slight PVG resistance influence on dynamic performance is evident too.

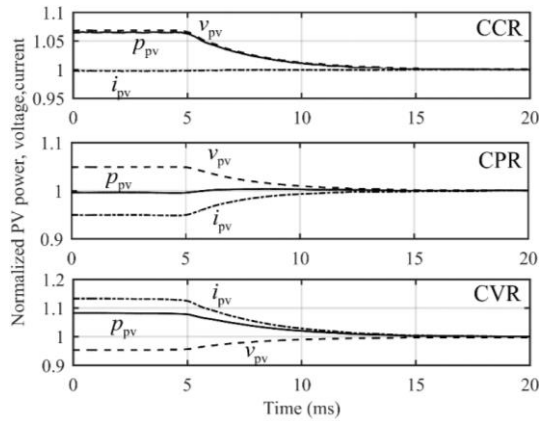


Fig. 11. Measured system responses of PVG voltage (dashed line), current (dash-dotted line), and power (solid line) to a PVG voltage reference step change under I-control.

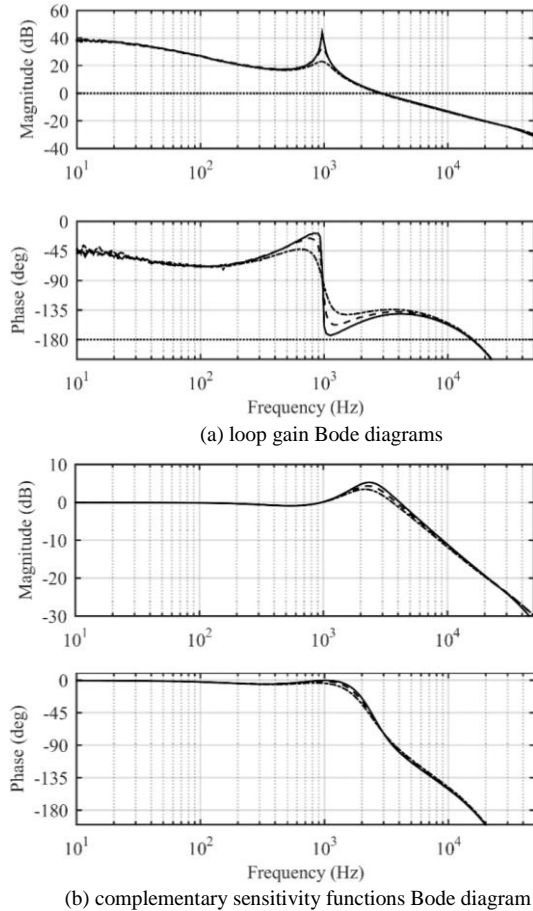


Fig. 12. Measured system responses under PID-control (CCR: solid line, CPR: dashed line, and CVR: dash-dotted line).

Fig. 13 presents measured PVG voltage, current, and power responses to a reference PVG voltage step change in the three operating regions under PID-control. The results also validate the high-order transient behavior which fits the performance predicted by (7).

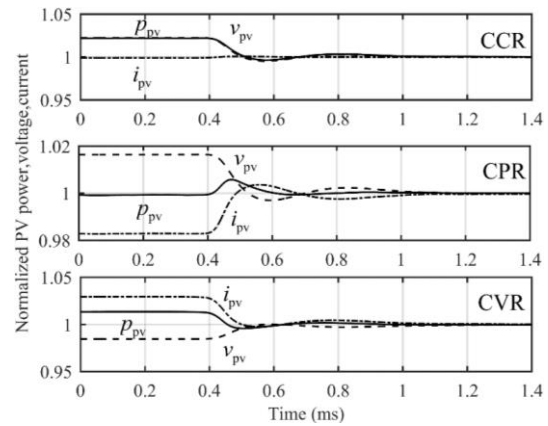


Fig. 13. Measured system responses of PVG voltage (dashed line), current (dash-dotted line), and power (solid line) to a PVG voltage reference step change under PID-control.

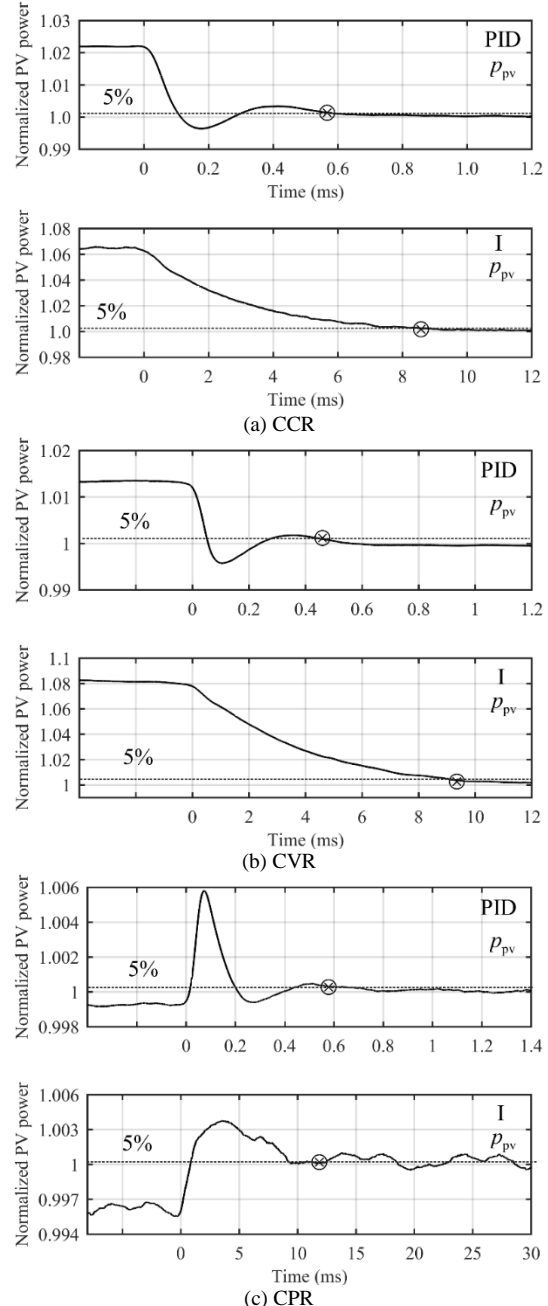


Fig. 14. Zoomed measured normalized transient responses of PVG power to a PVG voltage reference step change.

IEEE TRANSACTIONS ON POWER ELECTRONICS

In order to validate the PVG power settling times, required for perturbation frequency selection, Fig. 14 presents zoomed PVG power responses to PVG reference voltage step change in the three regions with 5% settling time marks. As indicated, settling times under I-control are 8.5 ms, 9.3 ms and 12 ms in CCR, CVR and CPR, respectively. Under PID-control, these are 0.55 ms, 0.45 ms and 0.6 ms in CCR, CVR and CPR, respectively. Comparing to (31) and (32), respectively, it may be concluded that settling times were accurately predicted analytically. Moreover, the settling time is the longest in CPR for both cases. It is important to emphasize that this is the consequence of additional factor of 2 in the natural logarithm of (17b) and (26b) rather than of PVG dynamic resistance influence.

VI. CONCLUSION

Perturbation frequency design plays an important role in direct MPPT algorithms, ensuring proper operation of the MPP tracker. While perturbation-frequency design rules for duty-ratio-operated MPPT converters are well developed, similar design rules for input-voltage-feedback-controlled MPPT processes are missing. This paper has introduced a method to estimate transient behavior of input-voltage-feedback-controlled MPPT converters for two typical design cases. In case of duty-ratio-operated MPPT converter, system power transient behavior is highly dependent on the operating point of photovoltaic generator. It was shown that such a dependence does not exist anymore when an input-voltage-feedback-controlled MPPT converter is used. Consequently, settling time is longest when the operating point resides in constant power region. Therefore, it is recommended to use the constant power region related equations to compute the settling time required for perturbation frequency determination in case of multi-loop MPPT structures, employing inner input voltage loop. In addition, settling time can be estimated accurately by means of the crossover frequency and phase margin of the input-voltage feedback loop only.

REFERENCES

- [1] S. Lyden and M. E. Haque, 'Maximum power point tracking techniques for photovoltaic systems: A comprehensive review and comparative analysis,' *Renew. Sustain. Energy Rev.*, vol. 52, pp. 1504-1518, Dec. 2015.
- [2] P.-C. Chen, P.-Y. Chen, Y.-H. Liu, et al., 'A comparative study of maximum power point tracking techniques for photovoltaic generation systems operating under fast changing environments,' *Solar Energy*, vol. 119, pp. 261-276, Sep. 2015.
- [3] N. Femia, G. Petrone, G. Spagnuolo, and M. Vitelli, 'Optimization of perturb and observe maximum power point tracking method,' *IEEE Trans. Power Electron.*, vol. 20, no. 4, pp. 963-973, Jul. 2005.
- [4] A. Ahmed, L. Ran, S. Moon, and J.-H. Park, 'A fast PV power tracking control algorithm with reduced power mode,' *IEEE Trans. Energy Convers.*, vol. 28, no. 3, pp. 565-575, Sep. 2013.
- [5] A. Sangwongwanich, Y. Yang, and F. Blaabjerg, 'High-performance constant power generation in grid-connected PV systems,' *IEEE Trans. Power Electron.*, vol. 31, no. 3, pp. 1822-1825, Mar. 2016.
- [6] Y. Yang, H. Wang, F. Blaabjerg, and T. Kerekes, 'Hybrid power control concept for PV inverters with reduced thermal loading,' *IEEE Trans. Power Electron.*, vol. 29, no. 12, pp. 6271-6275.
- [7] R. Tonkoski, L. A. C. Lopes, and T. H. M. El-Fouly, 'Coordinated active power curtailment of grid connected PV inverters for overvoltage prevention,' *IEEE Trans. Sustain. Energy*, vol. 2, no. 2, pp. 139-147, Apr. 2011.

- [8] N. Femia, G. Petrone, G. Spagnuolo, and M. Vitelli, *Power Electronics and Control Techniques for Maximum Power Harvesting in Photovoltaic Systems*, Boca Raton, FL, USA; CRC Press, 2013.
- [9] M. Balato, L. Costanzo and M. Vitelli, "Maximum power point tracking techniques," *Wiley Encyclopedia of Electrical and Electronics Engineering*, pp. 1-26, 2016.
- [10] S. Liu and R. A. Dougal, 'Dynamic multiphysics model for solar array,' *IEEE Trans. Energy Convers.*, vol. 17, no. 2, pp. 285-294, Jun. 2002.
- [11] L. Nousiainen, J. Puukko, A. Mäki, et al., 'Photovoltaic generator as an input source for power electronic converters,' *IEEE Trans. Power Electron.*, vol. 28, no. 6, pp. 3028-3028, Jun. 2013.
- [12] W. Xiao, W. G. Dunford, P. R. Palmer, and A. Capel, 'Regulation of photovoltaic voltage,' *IEEE Trans. Ind. Electron.*, vol. 54, no. 3, pp. 1365-1374, Jun. 2007.
- [13] T. Esram, J. W. Kimball, P. T. Krein, P. L. Chapman, and P. Midya, 'Dynamic maximum power point tracking of photovoltaic arrays using ripple correlation control,' *IEEE Trans. Power Electron.*, vol. 21, no. 5, pp. 1282-1291, Sept. 2006.
- [14] T. Suntio, J. Leppäaho, J. Huusari, and L. Nousiainen, 'Issues on solar-generator-interfacing with current-fed MPP-tracking converters,' *IEEE Trans. Power Electron.*, vol. 25, no. 9, pp. 2409-2419, Sep. 2010.
- [15] J. L. Wyatt and L. O. Chua, 'Nonlinear resistive maximum power theorem with solar cell application,' *IEEE Trans. Circuits. Syst.*, vol. Cas-30, no. 11, pp. 824-828, Nov. 1983.
- [16] A. Kuperman, M. Averbukh and S. Lineykin, "Maximum power point matching versus maximum power point tracking for solar generators," *Renew. Sustain. Energy Rev.*, vol. 19, pp. 11 - 17, 2013.
- [17] S. Gadelovits, M. Sitbon, T. Suntio and A. Kuperman, "Single-source multi-battery solar charger: case study and implementation issues," *Prog. Photovolt. Res. Appl.*, vol. 23, no. 12, pp. 1916 - 1928, Dec. 2015.
- [18] J. Viinamäki, J. Jokipii, T. Messo, M. Sitbon, and A. Kuperman, 'Comprehensive dynamic analysis of PV-generator-interfacing DC-DC boost-power-stage converter,' *IET Renew. Power Gener.*, vol. 9, no. 4, pp. 306-314, Apr. 2015.
- [19] M. Sitbon, J. Leppäaho, T. Suntio and A. Kuperman, 'Dynamics of photovoltaic generator interfacing voltage controlled buck power stage,' *IEEE J. Photovolt.*, vol. 5, no. 2, pp. 633 - 640, Mar. 2015.
- [20] J. Kivimäki, S. Kolesnik, M. Sitbon, T. Suntio and A. Kuperman, "Revisited perturbation frequency design guideline for direct fixed-step maximum power point tracking algorithms," *IEEE Trans. Ind. Electron.*, Accepted for publication.
- [21] N. Femia, G. Petrone, G. Spagnuolo, and M. Vitelli, 'A technique for improving P&O MPPT performance of double-stage grid-connected photovoltaic systems,' *IEEE Trans. Ind. Electron.*, vol. 56, no. 11, pp. 4473-4482, Nov. 2009.
- [22] R. P. Venturini, V.V. R. Scarpa, G. Spiazzi, and S. Buso, 'Analysis of limit cycle oscillations in maximum power point tracking algorithms,' in *Proc. IEEE PESC*, 2009, pp. 378-384.
- [23] A. Urtasun, P. Sanchis, and L. Marroyo, 'Adaptive voltage control of the DC/DC boost stage in PV converters with small input capacitor,' *IEEE Trans. Power Electron.*, vol. 28, no. 11, pp. 5038-5048, Nov. 2013.
- [24] M. Sitbon, S. Schacham, T. Suntio, and A. Kuperman, 'Improved adaptive input voltage control of a solar array interfacing current mode controlled boost power stage,' *Energy Convers. Manage.*, vol. 98, pp. 369-373, Jul. 2015.
- [25] S. Kolesnik, M. Sitbon, S. Gadelovits, T. Suntio and A. Kuperman, 'Interfacing renewable energy sources for maximum power transfer - Part II: Dynamics,' *Renew. Sustain. Energy Rev.*, vol. 51, pp. 1771 - 1783, 2015.
- [26] K. Ogata, *Modern Control Engineering*, Upper Saddle River, NJ, USA; Prentice-Hall, 1997.
- [27] N. Femia, D. Granozio, G. Petrone, G. Spagnuolo, and M. Vitelli, 'Predictive and adaptive MPPT perturb and observe method,' *IEEE Trans. Aerosp. Electron. Syst.*, vol. 43, no. 3, pp. 934-950, Jul. 2007.
- [28] G. Graditi, G. Adinolfi, N. Femia and M. Vitelli, "Comparative analysis of synchronous rectification boost and diode rectification boost converter for DMPPT applications," in *Proc. 20th IEEE Symp. Ind. Electron.*, Gdansk, Poland, pp. 1000-1005, Jun. 27-30, 2011.